Computational Exploration of NO Single-Site Disproportionation on Fe-MOF-5

Jesús Jover,*,[†,‡] Carl K. Brozek,[§] Mircea Dincă,[∥] and Núria López[‡]

[†]Secció de Química Inorgànica, Departament de Química Inorgànica i Orgànica and Institut de Química Teòrica i Computacional (IQTC-UB), Universitat de Barcelona, Martí i Franquès 1-11, 08028 Barcelona, Spain

[‡]Institute of Chemical Research of Catalonia, ICIQ, The Barcelona Institute of Science and Technology, BIST, Av. Països Catalans 16, 43007 Tarragona, Spain

[§]Department of Chemistry and Biochemistry, University of Oregon, Eugene, Oregon 97403, United States

[∥]Department of Chemistry, Massachusetts Institute of Technology, 77 Massachusetts Avenue, Cambridge, Massachusetts 02139, United States

Ⓢ *Supporting Information*

ABSTRACT: Nitric oxide disproportionation at the site-isolated Fe centers of the metal organic framework material known as Fe-MOF-5 has been explored with density functional theory (DFT). The computed reaction sequence supports the mechanism suggested by experiment that involves the formation of the monoanionic hyponitrite radical. The validity of the computed reaction mechanism is bolstered by impressive agreement between computed and experimental vibrational spectroscopic evidence of each reaction step. Similarly the analogous Mn^{II}-MOF-5 system indicates that the disproportionation of NO should proceed smoothly with this single-site material. These results, observed also for some homogeneous Mn(II) catalysts, indicate that heterogeneous Mn-based materials could be employed as efficient biological and industrial catalytic systems in NO disproportionation processes.
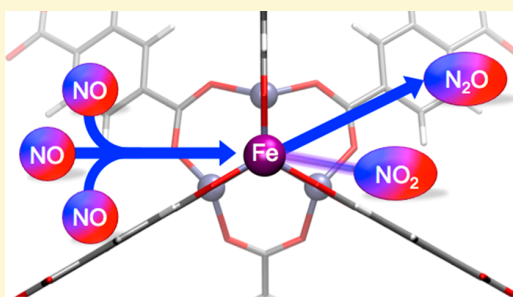
INTRODUCTION

Nitric oxide (NO) is one of the key intermediates formed in the denitrification processes of the global nitrogen cycle. In this natural cycle nitrogen is converted into different chemical species as it circulates through atmospheric, marine, and terrestrial ecosystems. The generation and decomposition of NO features prominently in diverse processes ranging from immune response to neurotransmission to blood pressure control.[1] The chemistry underlying these processes typically involves electron transfer between NO and transition metal centers.[2,3] Some of these redox reactions occur at the active sites of metalloenzymes such as nitric oxide (NOR) and flavodiiron protein (FDP) reductases.[4–9] Among these biological transformations, disproportionation of NO is particularly appealing because NO is one of the key components of N_xO_y species that pollute the atmosphere.[10] Reproducing NO disproportionation in synthetic systems for widespread deployment on an industrial scale for $deNO_x$ catalysis has been a longstanding challenge.[11,12] Fundamental research toward this goal has focused on using molecular transition metal-containing complexes to disproportionate NO into NO_2^- and N_2O or N_2 as a way to glean the precise structural and electronic factors key to maximizing catalytic activity in large-scale practical systems. Thus, far, transition metals reported to participate in NO disproportionation include Fe,[13–16]

Mn,[17–20] Ni,[21,22] Cu,[23–28] Ru,[29] Rh,[30] and Pd.[31] As molecular species these examples react under homogeneous conditions, whereas ideal $deNO_x$ catalysts should perform under heterogeneous conditions, in which the catalytic species would have improved activity, stability, and reusability. Very recently, crystalline materials have been targeted as single-site heterogeneous catalysts that take advantage of the specific steric and electronic advantages of molecular homogeneous systems.[32–36] In 2015, the first single-site heterogeneous material to promote disproportionation of NO into N_2O and NO_2^- was reported. It was based on an Fe(II)-exchanged variant of the ionic material known MOF-5, termed Fe-MOF-5. The reaction (Scheme 1) proceeded over the course of minutes under NO atmosphere at room temperature and could be monitored in situ by infrared spectroscopy, with each observed intermediate easily isolated for characterization by complementary techniques.[15]

The suite of experimental data supported the proposal of a reaction mechanism that proceeds through an unusual monoanionic hyponitrite radical ($N_2O_2^{•-}$). Although this species has been invoked in a variety of biological and
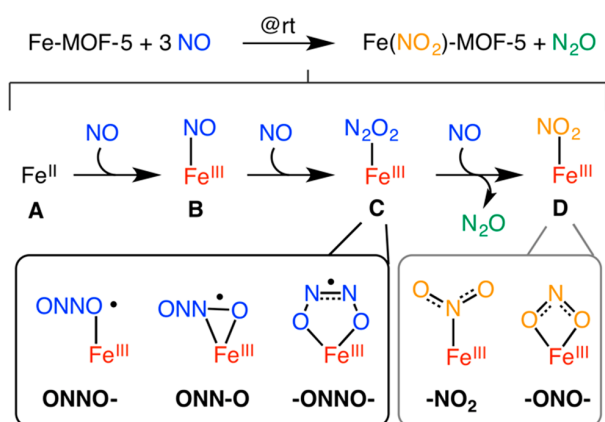
industrial transformations, it had never been stabilized indefinitely for further characterization.[37,38] Most plausible reaction mechanisms of NO disproportion involve the formation of a hyponitrite species, but whereas one route could involve spontaneous conversion of $N_2O_2^-$ to N_2O and a metal oxo, the evidence suggested an alternative route involving attack of NO at the $N_2O_2^-$ to form $N_3O_3^-$ that then released N_2O, leaving behind $Fe-NO_2$. The present computational work is focused on exploring the full reaction mechanism of NO disproportionation promoted by Fe-MOF-5, including the Fe-bound N_xO_y species not observed by vibrational spectroscopy. We proceed by determining the most favorable reaction sequence and then comparing calculated spectroscopic features to experiment. To expand the applicability of these results, we explore the ability of other MOF-5 variants including divalent cations such as Mn(II) and Co(II) for activity toward disproportionation of NO.

RESULTS AND DISCUSSION

Computed Reaction Mechanism. The computed reaction sequence for the NO disproportionation on Fe-MOF-5 is shown in Scheme 2. Fe-MOF-5 is a derivative of the parent

**Scheme 2. Computed Reaction Pathway for the Fe-MOF-5 Catalyzed NO Disproportionation**[a]
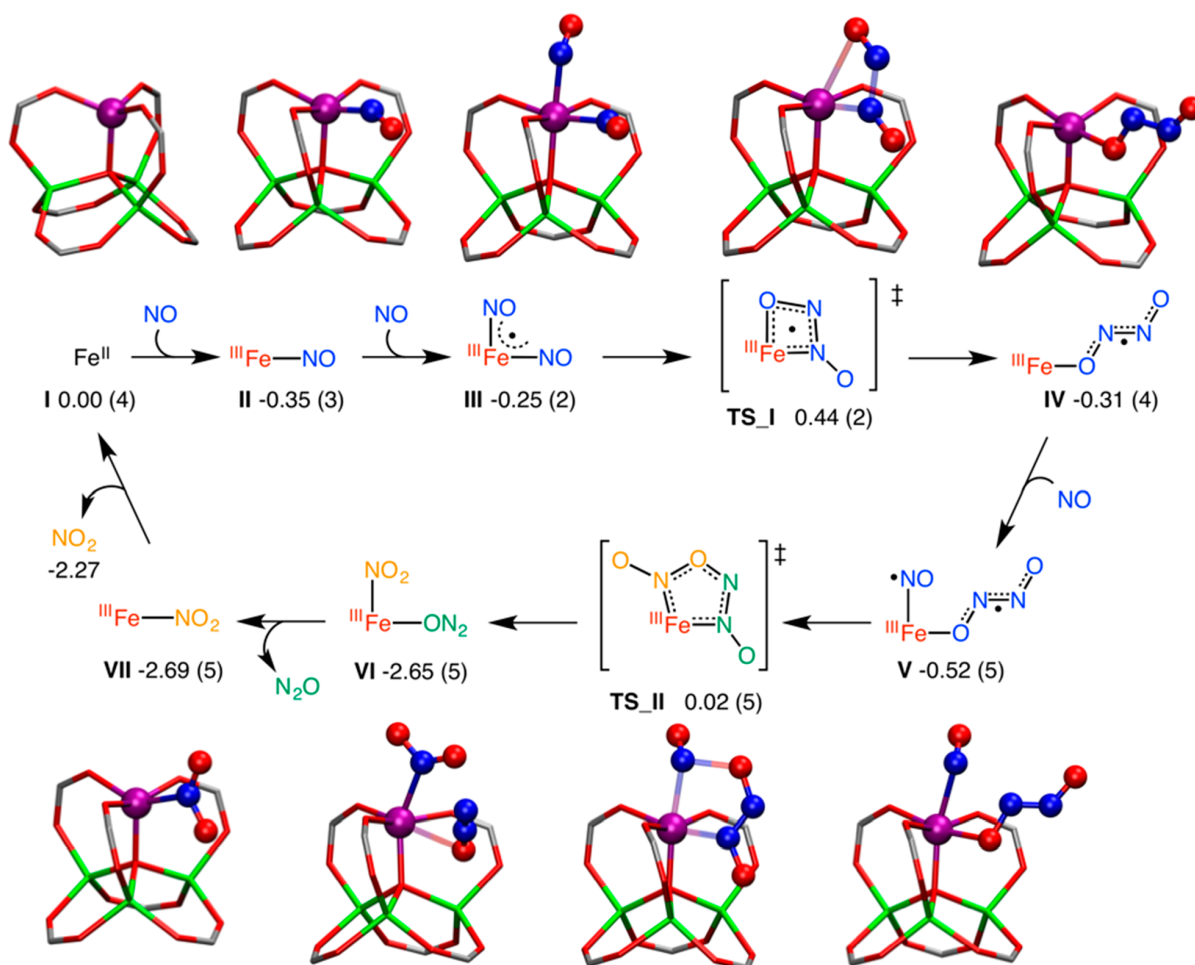
[a]Energies are given in eV, the number of unpaired electrons of each species is given between parentheses. Color code of the Fe core: C = gray, N = blue, O = red, Fe = purple, Zn = green; atoms represented as balls correspond to those actively participating in the reaction steps.

compound MOF-5 that can be prepared *via* postsynthetic partial ion metathesis of 25% of Zn with Fe.[39] The starting matrix MOF-5 shows a cubic crystal structure with $[Zn_4O\text{-}(BDC)_3]_8$ stoichiometry (BDC = 1,4-benzenedicarboxylate). In this structure, corners are built up of zinc oxide tetrahedral units, $[Zn_4O]^{6+}$, connected to each other by BDC ligands. The reaction pathway shown in Scheme 2 includes most of the structures proposed in the original experimental report and allows the rationalization of a great number of the experimental observations (*vide infra*). The reaction starts by the coordination of a NO molecule to the high-spin iron(II) center in Fe-MOF-5 (intermediate **I**).

There are two different possibilities for this process to take place, NO could bind onto either an axial or an equatorial position. The latter is slightly more favored, with an overall energy gain of 0.35 eV. Thus, in intermediate **II** the Fe atom displays a square pyramid structure in which the incoming NO lies *cis* to the central oxo group of the MOF core. The Fe−NO distance in this intermediate is as short as 1.83 Å and the Fe−N−O angle is 148.0°, quite far from a linear arrangement. These parameters agree with the expected one-electron transfer between iron and the incoming nitric oxide molecule, and therefore intermediate **II** should be classified as a Fe^{III}−NO^- species.[40] The addition of a second NO produces the dinitrosyl intermediate **III**, which is slightly higher in energy than the previous intermediate. In this case the iron center adopts an octahedral arrangement in which the incoming nitric oxide occupies the free axial coordination site. The Fe−NO distances in this structure are 2.10 and 2.00 Å, for the axial and equatorial NO groups, respectively. This seems to indicate that the coordination of the second NO ligand entails a certain degree of electron density transfer from the iron, which in turn produces the elongation of the previously formed Fe−NO bond. The reduction of the equatorial Fe−N−O angle to 135.4° seems also to support this fact. Overall, species **III** seems to have a delocalized unpaired electron between the iron(III) center and both NO groups. Once **III** has been obtained, the reaction proceeds by the formation of the hyponitrite species; this step involves the coupling of both coordinated nitrogen atoms and, presumably, happens through transition state **TS_I**. In this transition state the axial NO slightly slips from the metal to come close to the equatorial NO group. The final configuration shows that the Fe−N_{ax} distance increases from 2.10 to 2.98 Å while the N−N distance shortens to 1.96 Å. The Fe−N_{eq} distance in this species is 1.94 Å, slightly shorter than that found in the previous intermediate. The energy requirement for this stage is 0.69 eV, and the overall barrier up to this point is 0.79 eV. Other alternative transition states were sought, e.g. the triangular −Fe−N−N− species in which both N atoms remain attached to the iron center; but those showed higher energy requirements and were consequently discarded. After the N−N bond formation an equatorial N-bound hyponitrite species is obtained (**IV_N**, Scheme 3, top); nevertheless, this compound easily evolves into the η^1-terminal O-bound hyponitrite (**IV**), which is more stable by 0.12 eV. The Fe−O distance in **IV** is 1.98 Å, while the N−N distance is 1.28 Å. This value is slightly longer than that found in dianionic $ONNO^{2-}$ species in which the double N=N bond is found between 1.20 and 1.25 Å.[41] In contrast, in **IV_N** the Fe−N distance is 2.07 Å while the N−N distance is as long as 1.73 Å, much closer to that found in a single bond.[41] A third option consists of the formation of the 5-membered ring intermediate **IV_C** (Scheme 3, top), enabled by the

Scheme 3. Possible Isomeric Species of Compounds IV (top) and VII (bottom)[a]

IV -0.31 (4) **IV_N** -0.19 (4) **IV_C** -0.31 (4)

VII -2.69 (5) **VII_O** -2.44 (5)
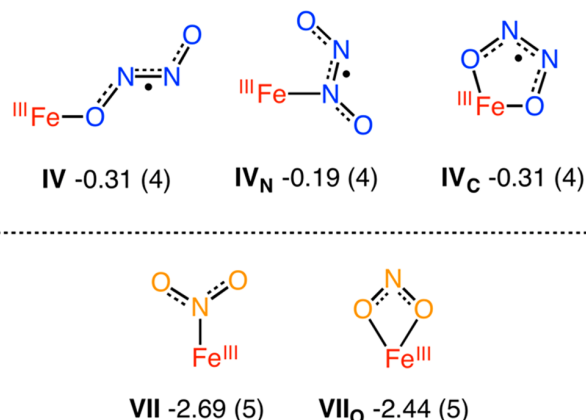
[a]Energies are given in eV and the number of unpaired electrons of each species is given between parentheses.

chelating ability of the hyponitrite substituent. Although the computed energy for this compound seems competitive, this possibility can be ruled out based on several observations. First of all, the direct formation of **IV_C** entails a cyclic transition state in which both O atoms are connected to the iron atom while the N−N bond is formed. The intermediate previous to this transition state, where both NO units are bound onto the iron center through the oxygen atoms, is higher in energy than **TS_I**, and consequently this pathway should be ruled out. Alternatively the Fe−ONNO− species (**IV_C**) could be formed by isomerization of the hyponitrite in compound **IV**. This process would imply a rearrangement of the ONNO moiety from *trans* to *cis*, which is blocked by the double bond nature of the N=N unit. A hypothetical transition state for this process was computed with the O−N−N−O dihedral angle fixed at 90°, and the relative energy value found for such species was as high as 0.91 eV, producing a much higher energy barrier of 1.26 eV.

After **IV** has been formed, the third NO substrate binds to the iron, occupying the free axial position and forming intermediate **V**. In this case the Fe−NO_{ax} distance is 2.30 Å while the Fe−$ONNO_{eq}$ distance slightly increases to 2.07 Å. The coordination of the NO moiety onto **IV** is energetically favored, and intermediate **V** is the most stable species (−0.52 eV) along the reaction pathway prior to the formation of the disproportionation products. Those species are obtained by the reaction between the coordinated hyponitrite and nitric oxide as shown in **TS_II** (Scheme 2). In order to react, the hyponitrite moiety rotates to coordinate to the iron center through one of the nitrogen atoms; this process takes the opposite terminal oxygen atom close to the axial NO group, where the attack takes place. In the transition state the Fe−N_{eq}, Fe−N_{ax}, and ON−ONNO distances are 2.07, 2.25, and 1.92 Å, respectively, while the distance of the breaking N−O bond slightly lengthens (1.33 Å vs 1.23 Å in intermediate **V**). This apparently complicated process requires only 0.54 eV to occur. Again, other possibilities were taken into consideration as alternatives to this transition state but none of them were compatible with getting to the final products. Once **TS_II** has been overcome, NO_2^- and N_2O are formed, and the system greatly stabilizes in energy (intermediate **VI**). N_2O is very weakly bound, the Fe−ON_2 distance is quite long (3.04 Å),

and thus it can be easily released without a remarkable change in the energy. The liberation of N_2O produces the high-spin $Fe^{III}-NO_2$ species as the final product of the reaction (**VII**). In this intermediate, the NO_2 substituent migrates to the energetically more favored equatorial position and the $Fe-NO_2$ distance becomes 2.13 Å. Alternatively, the chelating Fe^{III}-nitrito (**VII$_O$**, Scheme 3, bottom) compound could be obtained; this intermediate is, however, higher in energy than the nitro isomer and is probably not formed under the reaction conditions. Finally, it has to be noted that the recovery of the initial Fe-MOF-5 catalyst from species **VII** should be possible with a relatively low energy investment of 0.52 eV; nevertheless, this possibility was not addressed in the experimental report.

In the original NO disproportionation with Fe-MOF-5 report the authors propose the reaction is promoted by a mononuclear Fe(II) species, as shown here. Other alternatives could involve the participation of Zn centers to produce Zn−NO or $Fe/Zn-N_xO_y$ chelating species. While a complete exploration of these pathways has not been performed, some of these Zn-active species have been computed and found to produce higher energies than those shown in Scheme 2. In the same line, the—potentially—reversible terephthalate partial dissociation, previously described in similar MOF systems,[42−44] was taken into account. However, the calculations indicate this process would not be energetically competitive with the proposed catalytic cycle, and thus, this possibility was finally discarded. As stated above, **IV** might undergo an alternative conversion of the bound hyponitrite into N_2O and an iron(III)-oxo species. This pathway has been explored (Scheme 4), and based only on the computed energies it could not be discarded. Expelling N_2O from **IV** requires 0.65 eV (**TS_O**), which does not seem a large enough barrier to prevent this process, especially because the formation of the

Scheme 4. Proposed Reaction Pathways from Intermediate IV[a]
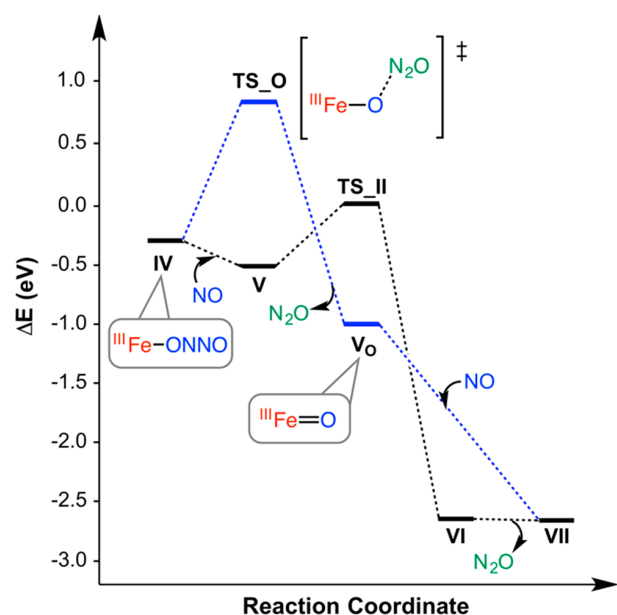
[a]Black line = pathway in Scheme 2; blue line = formation of iron-oxo intermediate (energies in eV).

Fe(III)-oxo compound (**V$_O$**) is thermodynamically favored. Nevertheless, in the presence of excess NO the reaction should happen preferentially by the pathway described above, and in that case, the barrier for producing **V$_O$** from **V** would rise to 0.86 eV. The addition of NO to **V$_O$**—if formed—automatically produces the final $Fe-NO_2$ (**VII**); all the attempts to compute a new species with an oxo group and nitric oxide on the iron center at the same time have ended up delivering this elimination product.

Connection between Experiments and Calculations. A vast amount of experimental data is available in the original report on the disproportionation reaction of NO with Fe-MOF-5.[15] A great deal of these data are focused on identifying the species produced during the reaction, and after an extensive analysis the reaction was postulated to proceed through the sequence shown in Scheme 1, where **B** should be the iron nitrosyl $\{FeNO\}^7$ adduct, **C** is a η^1-terminal iron(III) hyponitrite species ($Fe^{III}-ONNO$), and **D** corresponds to an N-bound Fe(III) nitro species. In this section the experimental results are combined with the DFT study in order to assess the computed reaction mechanism. In order to do this, the available experimental data will be compared to parameters directly obtained from the proposed species along the reaction pathway, i.e. DRIFTS vs computed IR spectra, and EXAFS (Figure S1) vs computed structural features. A summary of the comparable experimental and calculated data of the proposed intermediates formed along the reaction can be found in Table 1.

The starting Fe-MOF-5 species (**A**) can be easily identified as **I**. **A** was characterized as a species containing isolated high-spin Fe(II) centers; the calculations indicate that the S = 2 ferrous material is almost 1.5 eV lower in energy that the corresponding low-spin S = 0 analog. This should not be surprising because all the first row transition metals in a tetrahedral coordination environment present a small d-orbital splitting.

Species **B** is a bit harder to determine. In the experimental report this compound was assigned to be an iron nitrosyl $\{FeNO\}^7$ adduct; however, computationally this species could be either the nitrosyl (**II**) or dinitrosyl (**III**) derivative. The computed energies of these species are quite close, and thus, they could be considered to coexist under the reaction conditions. The experimental DRIFTS for species **B** shows the $\nu_{(N-O)}$ broad band centered at 1793 cm^{-1} with a small shoulder at lower wavenumbers (ca. 1760 cm^{-1}). The computed IR spectrum of **II** shows only one band close to that region (1778 cm^{-1}), but compound **III** displays two close bands, one medium band at 1714 cm^{-1} and a strong band at 1793 cm^{-1}, corresponding to the coupled symmetric and asymmetric $\nu_{(N-O)}$ vibrational modes of the NO groups, respectively. The overlap of those signals, which probably suffer some broadening, could produce the finally observed spectrum of species **B**.

Identification of **C** would probably be the most difficult one to undertake in this study; however, the outstanding experimental characterization allows the assignment of **C** as the $Fe^{III}-ONNO$ species. This statement can be confirmed through the calculation of the different hyponitrite species shown above. The EXAFS experiment rules out the possibility of the chelating $Fe^{III}(-ONNO-)$ hyponitrite (**IV$_C$**) to be species **C** because the iron center in this compound should have a coordination number of 5, and the distance between the metal and the fifth substituent should be close to 1.98 Å.

Table 1. Summary of Experimental and Calculated Data

Species	Experimental data		Calculated data		Assignment
	DRIFTS bands (cm^{-1})	EXAFS Fe–(N_xO_y) (Å)	IR bands (cm^{-1})	Computed Fe–(N_xO_y) (Å)	
B			$\nu_{(N-O)}$ 1778	1.83	Fe(NO) (**II**)
	$\nu_{(N-O)}$ 1793		$\nu_{(N-O)a}$ 1793 $\nu_{(N-O)s}$ 1714	2.00$_{(eq)}$2.10$_{(ax)}$	Fe(NO)$_2$ (**III**)
C	$\nu_{(N-N)}$ 1178 $\nu_{(N-O)}$ 868	1.98	$\nu_{(N-N)}$ 1111 $\nu_{(N-O)}$ 1012	1.98	Fe-ONNO (**IV**)
D	$\nu_{(N-O)}$ 1220 $\delta_{(O-N-O)}$ 797	2.08	$\nu_{(N-O)s}$ 1246 $\delta_{(O-N-O)}$ 758	2.13	Fe-NO$_2$ (**VII**)

Obviously, these requirements cannot be met by the chelating hyponitrite and thus the search is reduced to the other two options: the O- or N-bound η^1-hyponitrite isomers, i.e. the computed species **IV** and **IV$_N$**. The calculations above state that **IV$_N$** is formed in the first place during the reaction but it should end up evolving into **IV**, which is energetically more stable by 0.12 eV. These energy values are quite similar, and thus other criteria should be employed to computationally ascertain the nature of **C**. The Fe–O distance found in **IV$_N$** is 2.07 Å while in compound **IV** it is found to be 1.98 Å, a perfect match to the distance determined by EXAFS. In addition, the IR spectrum of **IV** resembles that obtained in the DRIFTS experiment.

For this compound four IR bands related to the hyponitrite substituent are found at 1453, 1111, 1012, and 690 cm^{-1}. The first, hidden in the DRIFTS spectra by the MOF vibrations, and the third bands correspond to the terminal and Fe-bound $\nu_{(N-O)}$ vibrations, respectively. The band found at 1111 cm^{-1} is related to the $\nu_{(N-N)}$ motion, and finally, the lowest energy band, which shows a very low absorption intensity, corresponds to a $\delta_{(ONNO)}$ wagging normal mode. The presence of the band at 1111 cm^{-1} seems to confirm intermediate **IV** as the experimental species **C**. On the other hand, the computed band at 1012 cm^{-1} shows a quite large shift toward higher energies for the Fe-bound $\nu_{(N-O)}$ vibrational mode when compared to the experimental DRIFTS. The computed IR spectra found for the other possible isomers of **C** show different features that do not comply with those observed in the experiments. For instance, compound **IV$_N$** shows three main bands related to the hyponitrite vibrations at 1606, 1563, and 701 cm^{-1}; these bands, especially the second one, are quite strong and correspond to the $\nu_{(N-O)a}$, $\nu_{(N-O)s}$, and $\nu_{(N-N)}$ vibrations, respectively. The IR spectrum for this species lacks the band observed experimentally at 1178 cm^{-1}, and hence, species **IV$_N$** can safely be discarded. The chelating hyponitrite species **IV$_C$** shows three hyponitrite-related IR stretching bands: $\nu_{(N-N)}$, $\nu_{(N-Oax)}$, and $\nu_{(N-Oeq)}$ at 1505, 965, and 775 cm^{-1}, respectively. Again, this intermediate does not show any signal near the DRIFTS band at 1178 cm^{-1} and, consequently, should be discarded.

EXAFS and Mössbauer (Figure S2) measurements indicate that species **D** is a high-spin pentacoordinated Fe^{III}–NO$_2$ species. The calculations of the plausible Fe–NO$_2$ (**VII**) and Fe–ONO– (**VII$_O$**) species indicate the species **D** has to be assigned to **VII** because it complies with all the experimental evidence. **VII** is lower in energy than **VII$_O$**, which also shows a wrong coordination number of 6. In **VII**, the Fe–N distance is slightly longer than that obtained in the experiments: 2.13 and 2.08 Å, respectively. In the case of **VII$_O$** both Fe–O distances present larger values of 2.17 (equatorial) and 2.20 (axial) Å, respectively. The computed IR spectrum of **VII** also serves to

confirm the identity of this intermediate, and the nitrite $\nu_{(N-O)a}$, $\nu_{(N-O)s}$, and $\delta_{(O-N-O)}$ bands appear at 1416, 1246, and 758 cm^{-1}. While the vibrations of the MOF lattice obscure the first one, the other two are pretty close to those obtained in the DRIFTS study (1220 and 797 cm^{-1}). In the case of species **VII$_O$** the IR spectrum shows the following bands: $\nu_{(N-O)a}$ 1230, $\nu_{(N-O)s}$ 1139, and $\delta_{(O-N-O)}$ 836 cm^{-1}, the second of which does not appear in the experiments although it should be observed based on the computed intensity.

The calculation of the IR spectra of the intermediates along the reaction allows the building of a simulated DRIFTS spectrum, which can be compared to that obtained in the original experiments (Figure 1). In order to build the computed DRIFTS only species **II**, **IV**, and **VII** have been taken into account since they have been identified as those observed in the experiments (see the Computational Details section for a description of this procedure). The experimental and simulated spectra are quite similar; at first, they both show the $\nu_{(N-O)}$ stretching of intermediate **B/II** at around 1790 cm^{-1}. This signal decays as the formation of the hyponitrite intermediate proceeds (**C/IV**), and the main $\nu_{(N-N)}$ band of this compound rises at around 1100 cm^{-1}; this value is slightly lower than that found in experiments, where the band is centered at around 1180 cm^{-1}. When the third NO reacts with the hyponitrite intermediate, the $\nu_{(N-O)}$ and $\delta_{(O-N-O)}$ bands of compound **D/VII** appear close to 1250 and 760 cm^{-1} while the signal of the former intermediate recedes to finally disappear. Of course, the agreement between experiments and calculations is not perfect and some discrepancies can be found. Some of them are due to the inherent differences between the experimental and computed systems; for instance, the bands obtained for the computed structures **IV** and **VII** around 1400–1500 cm^{-1} are not observed in the experimental DRIFTS because of the strong phenyl C–C absorption bands. A similar effect is observed in the $\nu_{(C-O)}$ bands of the carboxylate groups, where the experimental signals appear at higher wavenumbers for the experimental study (1600–1700 cm^{-1}) when compared to the smaller computed system (1550–1600 cm^{-1}). Additionally, in the computed spectra the experimental band at 785 cm^{-1}, corresponding to the formation of **C/IV**, cannot be observed, probably because the computed intensity is too low. Finally, in the experimental spectra there is a band assigned to compound **D/VII** located at 1000 cm^{-1} that cannot be interpreted with the calculations because the only computed signal to appear in that region corresponds to the $\nu_{(N-O)}$ signal of compound **C/IV**, which displays a very poor intensity.

Finally, the experimental data indicates that the rate constant of the disproportionation reaction, which is carried out at room temperature, should be lower than 0.01 s^{-1} for the rate-determining step. This value, when translated to an energy
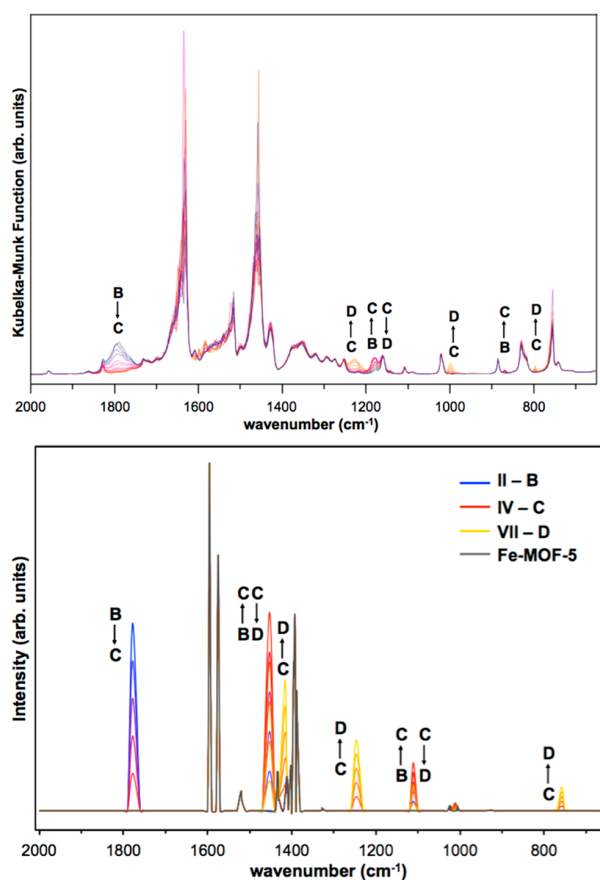
Figure 1. Experimental (top) and simulated (bottom) DRIFTS spectra of Fe-MOF-5 in the presence of NO. Spectra begin with species **B/II** (blue), which transforms into **C/IV** (red) and into **D/VII** (gold). The computed bands of Fe-MOF-5 are shown in gray. The experimental DRIFTS spectrum adapted with permission from *J. Am. Chem. Soc.* **2015**, 137, 7495−7501. Copyright 2015 American Chemical Society.

value by means of the Eyring−Polanyi equation, affords a minimum activation barrier of 0.87 eV. The computed energy barrier for the overall reaction, which corresponds to the energy difference between intermediate **II** and **TS_I**, is 0.79 eV, slightly lower but still close to the minimum value inferred from the experimental data.
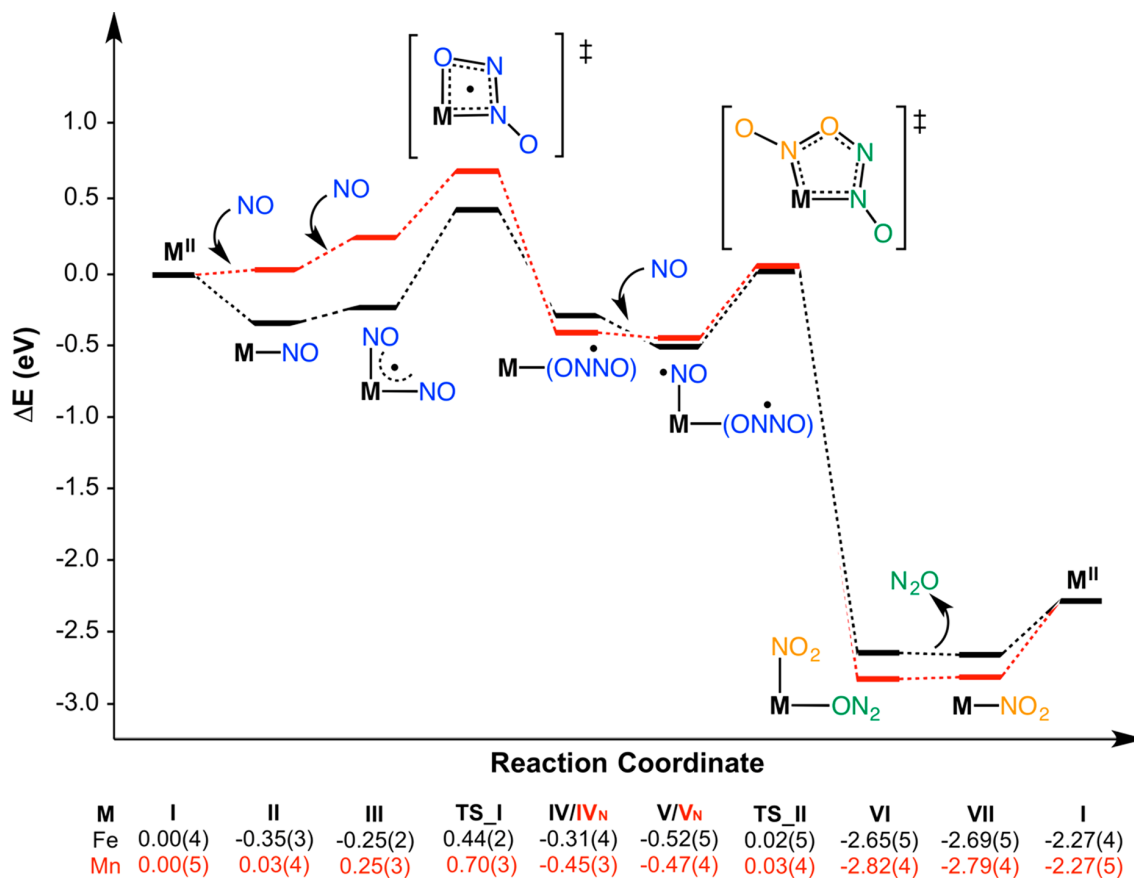
Extension to Other M^{II}-Doped MOF-5 Systems. Once the exploration of the NO disproportionation reaction with Fe-MOF-5 has been completed, the computed mechanism has been extended, carrying out the same set of calculations, to other transition metal-doped MOF-5 analogues. At first, two more metals were taken into consideration: Mn(II) and Co(II); and thus the reaction sequence shown in Scheme 2 was computed for both of them. There are experimental reports, most of those involving mononuclear manganese species,[17−20] showing that manganese should be able to engage in the NO disproportionation; on the other hand, cobalt has not been reported before to participate in such a process. Additionally, Mn-MOF-5 has been already prepared and employed in catalytic reactions,[39,45] and thus it should be possible to test experimentally in case the computed results are encouraging. Unfortunately, the DFT study of the Co-MOF-5 system could not be achieved because many times it was not

possible to find a stable electronic/geometric solution; that is, optimizations often ended up in dissociated species. Consequently, the cobalt-doped system was finally discarded. In contrast, the Mn-MOF-5 platform provides robust electronic state solutions and the calculations indicate that the disproportionation of NO should be possible with this catalyst. The computed energies for the Mn-MOF-5 system are shown in Scheme 5 along with those obtained for Fe-MOF-5. The computed magnetization values and the Bader charges for Mn and the N_xO_y fragments can be found in Table S2. As may be observed, the potential energy profile for Mn(II) shows the same trend as that obtained for Fe(II), although in the case of the former the binding of the first two NO molecules is less favored; that is, the formation of intermediates **II** and **III** in the Mn-MOF-5 system requires a small investment of energy. Nevertheless, the transition state leading to the hyponitrite intermediate with Mn is not very demanding, and thus the barrier to furnish the N−N bond, computed as the energy difference between Mn-MOF-5 + 2NO and **TS_I**, is 0.70 eV, in contrast with the 0.79 eV computed for Fe-MOF-5. In this case, the most stable hyponitrite species corresponds to intermediate **IV$_N$**, with an overall computed energy of −0.45 eV and a Mn−N distance of 2.22 Å. The terminal Mn-ONNO (**IV**) compound is higher in energy (−0.14 eV) while the chelating **IV$_C$** intermediate is found at −0.36 eV. The formation of this latter compound, by rotating around the N−N bond, should be plausible because the N−N distance in **IV$_N$** (1.69 Å) seems closer to a single bond character. After the obtention of **IV$_N$** the reaction proceeds by addition of the third NO substrate, which attaches onto the free axial position of manganese, while the hyponitrite remains connected to the metal through the N atom in an equatorial site (**V$_N$**). In this case the Mn−N$_{eq}$ and Mn−N$_{ax}$ are very similar, 2.22 and 2.24 Å, respectively. The formation of **V$_N$** takes the energy slightly down to a relative value of −0.47 eV, which corresponds to the lowest energy value so far. This architecture has also been computed for the Fe-MOF-5 system and found to lie at a slightly higher energy value than intermediate **V**. Finally, the reaction between the Mn-bound NO and hyponitrite substituents affords N_2O and the final Mn^{III}−NO$_2$ species (**VII**). This step requires 0.50 eV to occur, which is a very similar value to that found for the Fe-MOF-5 system, and states that the overall barrier of the disproportionation process corresponds to the formation of the hyponitrite intermediate with a value of 0.70 eV. As in the case of Fe-MOF-5, the Mn-ONO- (**VII$_O$**) alternative nitrito species was also computed and found to be slightly higher in energy than the nitro isomer: −2.39 vs −2.25 eV for **VII** and **VII$_O$**, respectively. In conclusion, the DFT calculations on the NO disproportion promoted by Mn-MOF-5 indicate that the reaction should be possible and probably faster than with the Fe-MOF-5 analog. This mechanism should also be considered as a serious candidate to explain the NO disproportion promoted by flexible Mn homogeneous systems such as those reported by Lippard in the late 1990s.[17]

■ CONCLUSIONS

The reaction mechanism of the NO disproportionation on Fe-MOF-5 has been successfully characterized by computational means. The study allows the identification of the species formed along the reaction course, which are in very good agreement with those proposed in the original experimental report. The computed mechanism states that the reaction

Scheme 5. Relative Energy Profiles for the Fe- and Mn-MOF-5 Catalyzed NO Disproportionation[a]

M	I	II	III	TS_I	IV/IV$_N$	V/V$_N$	TS_II	VI	VII	I
Fe	0.00(4)	-0.35(3)	-0.25(2)	0.44(2)	-0.31(4)	-0.52(5)	0.02(5)	-2.65(5)	-2.69(5)	-2.27(4)
Mn	0.00(5)	0.03(4)	0.25(3)	0.70(3)	-0.45(3)	-0.47(4)	0.03(4)	-2.82(4)	-2.79(4)	-2.27(5)

[a]M: Fe = black, Mn = red, energies in eV, unpaired electrons are given between parentheses.

proceeds by the binding of two NO substrates onto the initial catalyst, the formation of a η^1-ONNO hyponitrite intermediate, and the subsequent coordination of a third NO substrate that reacts with the O-bound hyponitrite to produce N_2O and an Fe^{III}–NO_2 bound species. The simulated IR spectra obtained from the computed geometries show a very good agreement with the bands observed during the experimental DRIFTS monitoring, confirming the identity of the species formed during the reaction. The computed structural features and the experimental EXAFS data are also in very good agreement, which positively contributes in the identification of Fe-bound hyponitrite and N-nitrito species.

Subsequently, the computed mechanism has been extended to explore whether other first-row divalent transition metals could be employed in Mn-MOF-5 systems to promote the NO disproportionation. The calculations involving Co(II) did not provide any useful information; on the other hand, the Mn-MOF-5 catalyst should be able to disproportionate NO. The computed barrier found for this system is lower than that found for the original Fe-MOF-5 material, indicating that the manganese analog should produce a faster reaction rate even though its NO adsorption properties are slightly poorer.

Overall, the flexibility of the MOF system, combined with the ability of the transition metal to produce stable structures with different coordination numbers, seems to be the key for producing an NO disproportionation operative platform. This kind of chemical behavior could probably be extended to other

low coordinate divalent iron and manganese flexible MOFs, which should be able to engage in similar NO abatement reactions and hence open new research opportunities in deNO$_x$ chemistry.

■ COMPUTATIONAL DETAILS

All calculations have been carried out at the DFT+U level as implemented in the VASP plane wave code, version 5.2.[46,47] The exchange-correlation functional developed by Perdew–Burke–Ernzerhof (PBE),[48] in combination with an effective U term (U$_{eff}$)[49] of 3.5 for Fe and 3.0 eV Co and Mn, respectively, was employed in the calculations. These settings have already been reported to correctly reproduce important properties such as binding energies.[50−52] Inner electrons were replaced by all-electron frozen cores PAW,[53,54] whereas valence electrons were expanded in plane waves with a cutoff energy of 450 eV. Geometries were optimized at the Γ point until the force threshold of 0.015 eV/Å was reached. Long-range dispersion contributions to the energies were included via the Grimme DFT-D2 correction.[55] Different spin states have been evaluated for most of the intermediates along the reaction pathways, but only the most stable ones are shown along the main text; however, in practically all the cases the calculations show that the most stable compounds are those in which the metal stays in a high-spin configuration, regardless of its coordination environment. Transition states were located with the climbing image nudged elastic band method and successively refined via standard procedures.[56] Initially, an analogous DFT methodology (PBE/PAW) was employed to model the reaction mechanism; however, these settings were found to produce results that were in clear disagreement with the experimental data; that is, species such as Fe-NO$_2$ (**VII**) were found to be more

stable in their low spin form, while experimentally **VII** has been characterized as a high spin N-bound nitrito compound. These errors can be related to the nature of the GGA functional employed, and we decided that using the DFT+U methodology could compensate this behavior. The U parameter was subsequently optimized by comparing the relative energies of the high spin $Fe-NO_2$ (**VII**) and chelating Fe-ONO- (**VII$_O$**) species in calculations ranging from 3.0 to 5.0 eV in 0.5 eV steps. The relative energy of these intermediates switches when the U parameter increases; that is, at higher U values **VII$_O$** is favored while lower U values produce a more stable **VII** species. Since **VII** is observed experimentally, we decided to stop the optimization procedure at a point fulfilling this condition but close to the crossing, which happened at U = 3.5 eV.

The DFT+U methodology is one of the suitable approaches to reduce the electronic self-interaction error in DFT studies[57−63] and has been largely applied by the solid state community as a mimic for hybrid functionals.[64−68] However, the DFT+U methodology is not free of errors and the quality of electron localization/delocalization[64,68,69] and the adequacy of the energetics/densities balance when compared to more accurate methods[69−72] have been called into question. Another possible source of error in DFT + U calculations can be the lack of static correlation treatment.[69] In principle, multireferential character could be expected to appear in the studied compounds, mainly due to the partially filled d-orbitals of the metal center and the radical character of NO, which could produce mixed low-energy states. However, the computed species herein are too large to carry out a complete multirefential study with e.g. CASSCF/CASPT2 calculations. Multireferential calculations using the Orca[73] package were attempted for describing the electronic structure of the cluster analog of the $Fe(NO)_2$ (**III**) compound (see below); nevertheless, the complex structure of this system, where unpaired electrons can be found on both the metal and the NO ligands, provided unconvincing results even when trying different active spaces. Monodeterminantal calculations on molecular clusters of different species were also computed with Gaussian09[74] using the def2-tzvp basis set[75] and the PBE,[48] PBE0,[48,76,77] and B3LYP[78−80] density functionals. These calculations show that, in all cases, the iron center remains in a high spin state and in the case of the hybrid functionals by a similar energy margin (ca. 1 eV) to that found in the DFT+U periodic calculations. Thus, multireference effects should not be expected to have a strong impact in the calculations.

The lattice parameter for MOF-5 was computed to be 13.070 Å with the aforementioned DFT+U methodology, in excellent agreement with the experimental value of 12.909 Å available from X-ray crystallography.[81] In this optimized cell, one Zn atom was replaced with Fe, and the structure was fully reoptimized. The final computed system contains two tetrahedral cores $[FeZn_3O(BDC)_3][Zn_4O-(BDC)_3]$ (BDC = 1,4-benzenedicarboxylate) and has a Fe:Zn ratio of 1:8 (12.5%). The replacement of any other Zn center by Fe is not necessary since the experimental magnetic susceptibility measurements indicate that Fe-MOF-5 features isolated S = 2 ferrous ions.[15]

The energies of the molecular species, namely NO, N_2O, and NO_2, have been corrected to include the corresponding zero-point energy and the translational entropy at 298 K. Both these values have been obtained from calculations with Gaussian09,[74] employing the PBE functional[48] along the 6-31G* basis set.[82−84] Additionally, the cyclic intermediates (namely **IV$_C$**, **VII$_O$**, **TS_I**, and **TS_II**) have been corrected to include the entropy loss upon cyclization, which amounts to 0.06 eV per bond at 298 K.[85]

The simulated IR spectra of the different Fe-MOF-5−N_xO_y have been obtained using the optimized plane wave calculations as starting point. The corresponding iron clusters have been extracted for each compound, and the phenyl rings have been replaced by methyl groups; hence, in these calculations the Fe-MOF-5 core structure is $[FeZn_3O(OAc)_6]$. Finally the modified carboxylate groups have been allowed to relax in a partial optimization of the geometry where the Fe atom and the N_xO_y units have been kept frozen. The IR spectra have been obtained with Gaussian09,[74] using the PBE functional[48] along with the def2-tzvp basis set,[75] and the final DRIFTS spectra have been

constructed by representing the characteristic bands of the involved species in increasing and decreasing percentages in each reaction step.

Calculating quantitatively precise partial charges and electron distributions in solids, which may be helpful in this study, has been demonstrated to be a difficult process.[86] However, we were able to compute the magnetization and Bader partial charges for all the species along the reaction sequence in order to ascertain the electron transfer processes between, mainly, the iron center and the N_xO_y moieties (Table S1). As expected, these computed quantities do not show a quantitative agreement with their expected magnetization values or formal oxidation states, preventing their usage as a clear criterion for describing the electron transfer processes in the studied reaction. Nevertheless, the computed parameters in Table S1 show a relatively good qualitative trend for the studied disproportionation reaction; that is, when iron(II) reacts with NO an evaluating increase in the computed Bader charge for Fe is observed while nitric oxide adopts an overall negative charge. This same behavior is also observed in computed Bader charges obtained from cluster calculations of reaction intermediates; on the other hand, other different methods for obtaining the atomic partial charges from molecular species (Mulliken, APT, and NBO) show a much worse agreement with the expected formal oxidation state for iron.

■ ASSOCIATED CONTENT

ⓢ Supporting Information

Computed energy terms, magnetization values, Bader charges, and fractional coordinates of the optimized species (PDF)

■ AUTHOR INFORMATION

Corresponding Author
*E-mail: jesus.jover@qi.ub.es.
ORCID ⓘ
Jesús Jover: 0000-0003-3383-4573
Núria López: 0000-0001-9150-5941

Notes
The authors declare no competing financial interest.
The computational data can be freely accessed through the ioChem-BD repository: DOI: 10.19061/iochem-bd-1-130.

■ ACKNOWLEDGMENTS

■ REFERENCES

(1) Ignarro, L.; Freeman, B. *Nitric Oxide: Biology and Pathobiology*, 3rd ed.; Academic Press: San Diego, CA, 2017.

(2) Hayton, T. W.; Legzdins, P.; Sharp, W. B. Coordination and Organometallic Chemistry of Metal−NO Complexes. *Chem. Rev.* **2002**, *102*, 935−992.

(3) Lee, D.-H.; Mondal, B.; Karlin, K. D., Nitrogen Monoxide and Nitrous Oxide Binding and Reduction. In *Activation of Small Molecules: Organometallic and Bioiniroganic Perspectives*; 2006; pp 43−79.

(4) Wasser, I. M.; de Vries, S.; Moënne-Loccoz, P.; Schröder, I.; Karlin, K. D. Nitric Oxide in Biological Denitrification: Fe/Cu Metalloenzyme and Metal Complex NOx Redox Chemistry. *Chem. Rev.* **2002**, *102*, 1201−1234.

(5) Silaghi-Dumitrescu, R.; Ng, K. Y.; Viswanathan, R.; Kurtz, D. M. A Flavo-Diiron Protein from Desulfovibrio vulgaris with Oxidase and Nitric Oxide Reductase Activities. Evidence for an in Vivo Nitric Oxide Scavenging Function. *Biochemistry* **2005**, *44*, 3572−3579.

(6) Collman, J. P.; Yang, Y.; Dey, A.; Decréau, R. A.; Ghosh, S.; Ohta, T.; Solomon, E. I. A functional nitric oxide reductase model. *Proc. Natl. Acad. Sci. U. S. A.* **2008**, *105*, 15660.

(7) Hayashi, T.; Caranto, J. D.; Wampler, D. A.; Kurtz, D. M.; Moënne-Loccoz, P. Insights into the Nitric Oxide Reductase Mechanism of Flavodiiron Proteins from a Flavin-Free Enzyme. *Biochemistry* **2010**, *49*, 7040−7049.

(8) Wang, J.; Schopfer, M. P.; Puiu, S. C.; Sarjeant, A. A. N.; Karlin, K. D. Reductive Coupling of Nitrogen Monoxide (•NO) Facilitated by Heme/Copper Complexes. *Inorg. Chem.* **2010**, *49*, 1404−1419.

(9) Hayashi, T.; Caranto, J. D.; Matsumura, H.; Kurtz, D. M.; Moënne-Loccoz, P. Vibrational Analysis of Mononitrosyl Complexes in Hemerythrin and Flavodiiron Proteins: Relevance to Detoxifying NO Reductase. *J. Am. Chem. Soc.* **2012**, *134*, 6878−6884.

(10) Lelieveld, J.; Crutzen, P. J. Role of Deep Cloud Convection in the Ozone Budget of the Troposphere. *Science* **1994**, *264*, 1759.

(11) Kim, M. H.; Nam, I.-S. In *Catalysis*; Spivey, J. J., Ed.; The Royal Society of Chemistry: Cambridge, 2005; Vol. *18*.

(12) *Past and present in DeNOx catalysis. From molecular modelling to chemical engineering*; Granger, P., Pârvulescu, V. I., Eds.; Elsevier: Oxford, 2007; Vol. *171*.

(13) Franz, K. J.; Lippard, S. J. NO Disproportionation Reactivity of Fe Tropocoronand Complexes. *J. Am. Chem. Soc.* **1999**, *121*, 10504−10512.

(14) Patra, A. K.; Rose, M. J.; Olmstead, M. M.; Mascharak, P. K. Reactions of Nitric Oxide with a Low-Spin Fe(III) Center Ligated to a Tetradentate Dicarboxamide N4 Ligand: Parallels between Heme and Non-heme Systems. *J. Am. Chem. Soc.* **2004**, *126*, 4780−4781.

(15) Brozek, C. K.; Miller, J. T.; Stoian, S. A.; Dincǎ, M. NO Disproportionation at a Mononuclear Site-Isolated Fe^{2+} Center in Fe^{2+}-MOF-5. *J. Am. Chem. Soc.* **2015**, *137*, 7495−7501.

(16) Confer, A. M.; McQuilken, A. C.; Matsumura, H.; Moënne-Loccoz, P.; Goldberg, D. P. A Nonheme, High-Spin {FeNO}^{8} Complex that Spontaneously Generates N$_2$O. *J. Am. Chem. Soc.* **2017**, *139*, 10621−10624.

(17) Franz, K. J.; Lippard, S. J. Disproportionation of Nitric Oxide Promoted by a Mn Tropocoronand. *J. Am. Chem. Soc.* **1998**, *120*, 9034−9040.

(18) Martirosyan, G. G.; Azizyan, A. S.; Kurtikyan, T. S.; Ford, P. C. Low temperature NO disproportionation by Mn porphyrin. Spectroscopic characterization of the unstable nitrosyl nitrito complex Mn^{III}(TPP)(NO)(ONO). *Chem. Commun.* **2004**, 1488−1489.

(19) Filipović, M. R.; Duerr, K.; Mojović, M.; Simeunović, V.; Zimmermann, R.; Niketić, V.; Ivanović-Burmazović, I. NO Dismutase Activity of Seven-Coordinate Manganese(II) Pentaazamacrocyclic Complexes. *Angew. Chem., Int. Ed.* **2008**, *47*, 8735−8739.

(20) Jiang, M.-X.; Liu, C.-G. Reduction of NO to N2O Catalyzed by a Mn-Substituted Keggin-Type Polyoxometalate: A Density Functional Theory Study. *J. Phys. Chem. C* **2017**, *121*, 12735−12744.

(21) Wright, A. M.; Wu, G.; Hayton, T. W. Formation of N$_2$O from a Nickel Nitrosyl: Isolation of the cis-[N$_2$O$_2$]$^{2−}$ Intermediate. *J. Am. Chem. Soc.* **2012**, *134*, 9930−9933.

(22) Wright, A. M.; Zaman, H. T.; Wu, G.; Hayton, T. W. Mechanistic Insights into the Formation of N$_2$O by a Nickel Nitrosyl Complex. *Inorg. Chem.* **2014**, *53*, 3108−3116.

(23) Ruggiero, C. E.; Carrier, S. M.; Tolman, W. B. Reductive Disproportionation of NO Mediated by Copper Complexes: Modeling N$_2$O Generation by Copper Proteins and Heterogeneous Catalysts. *Angew. Chem., Int. Ed. Engl.* **1994**, *33*, 895−897.

(24) Schneider, J. L.; Carrier, S. M.; Ruggiero, C. E.; Young, V. G.; Tolman, W. B. Influences of Ligand Environment on the Spectroscopic Properties and Disproportionation Reactivity of Copper−Nitrosyl Complexes. *J. Am. Chem. Soc.* **1998**, *120*, 11408−11418.

(25) Shimokawabe, M.; Okumura, K.; Ono, H.; Takezawa, N. N$_2$O and NO$_2$ Formation in the Disproportionation of NO over Ion Exchanged Cu-ZSM-5 at Lower Temperature. *React. Kinet. Catal. Lett.* **2001**, *73*, 267−274.

(26) Lionetti, D.; de Ruiter, G.; Agapie, T. A trans-Hyponitrite Intermediate in the Reductive Coupling and Deoxygenation of Nitric Oxide by a Tricopper−Lewis Acid Complex. *J. Am. Chem. Soc.* **2016**, *138*, 5008−5011.

(27) Metz, S. N$_2$O Formation via Reductive Disproportionation of NO by Mononuclear Copper Complexes: A Mechanistic DFT Study. *Inorg. Chem.* **2017**, *56*, 3820−3833.

(28) Wijeratne, G. B.; Hematian, S.; Siegler, M. A.; Karlin, K. D. Copper(I)/NO(g) Reductive Coupling Producing a trans-Hyponitrite Bridged Dicopper(II) Complex: Redox Reversal Giving Copper-(I)/NO(g) Disproportionation. *J. Am. Chem. Soc.* **2017**, *139*, 13276−13279.

(29) Azizyan, A. S.; Kurtikyan, T. S.; Martirosyan, G. G.; Ford, P. C. Tracking Reactive Intermediates by FTIR Monitoring of Reactions in Low-Temperature Sublimed Solids: Nitric Oxide Disproportionation Mediated by Ruthenium(II) Carbonyl Porphyrin Ru(TPP)(CO). *Inorg. Chem.* **2013**, *52*, 5201−5205.

(30) Gaviglio, C.; Pellegrino, J.; Milstein, D.; Doctorovich, F. NO disproportionation by a {RhNO}^{9} pincer-type complex. *Dalton Trans.* **2017**, *46*, 16878−16884.

(31) Stromnova, T. A.; Shishilov, O. N.; Churakov, A. V.; Kuz'mina, L. G.; Howard, J. A. K. NO-disproportionation, promoted by Pd-cluster: formation and X-ray structure of Pd$_8$(μ-CO)$_4$(μ-OOCC-Me$_3$)$_8$[μ-N(=O)O−]$_4$. *Chem. Commun.* **2007**, 4800−4802.

(32) Rogge, S. M. J.; Bavykina, A.; Hajek, J.; Garcia, H.; Olivos-Suarez, A. I.; Sepúlveda-Escribano, A.; Vimont, A.; Clet, G.; Bazin, P.; Kapteijn, F.; Daturi, M.; Ramos-Fernandez, E. V.; Llabrés i Xamena, F. X.; Van Speybroeck, V.; Gascon, J. Metal−organic and covalent organic frameworks as single-site catalysts. *Chem. Soc. Rev.* **2017**, *46*, 3134−3184.

(33) Chen, Z.; Vorobyeva, E.; Mitchell, S.; Fako, E.; Ortuño, M. A.; López, N.; Collins, S. M.; Midgley, P. A.; Richard, S.; Vilé, G.; Pérez-Ramírez, J. A heterogeneous single-atom palladium catalyst surpassing homogeneous systems for Suzuki coupling. *Nat. Nanotechnol.* **2018**, *13*, 702−707.

(34) Cui, X.; Li, W.; Ryabchuk, P.; Junge, K.; Beller, M. Bridging homogeneous and heterogeneous catalysis by heterogeneous single-metal-site catalysts. *Nat. Catal.* **2018**, *1*, 385−397.

(35) Li, F.; Chen, Z. Cu dimer anchored on C2N monolayer: low-cost and efficient Bi-atom catalyst for CO oxidation. *Nanoscale* **2018**, *10*, 15696−15705.

(36) Tian, S.; Wang, Z.; Gong, W.; Chen, W.; Feng, Q.; Xu, Q.; Chen, C.; Chen, C.; Peng, Q.; Gu, L.; Zhao, H.; Hu, P.; Wang, D.; Li, Y. Temperature-Controlled Selectivity of Hydrogenation and Hydro-deoxygenation in the Conversion of Biomass Molecule by the Ru1/mpg-C3N4 Catalyst. *J. Am. Chem. Soc.* **2018**, *140*, 11161−11164.

(37) Poskrebyshev, G. A.; Shafirovich, V.; Lymar, S. V. Hyponitrite Radical, a Stable Adduct of Nitric Oxide and Nitroxyl. *J. Am. Chem. Soc.* **2004**, *126*, 891−899.

(38) Halliwell, B.; Gutteridge, M. C. *Free radicals in biology & medicine*, 5th ed.; Oxford University Press: Oxford, 2015.

(39) Brozek, C. K.; Dincǎ, M. Ti^{3+}-, V$^{2+/3+}$-, Cr$^{2+/3+}$-, Mn^{2+}-, and Fe^{2+}-Substituted MOF-5 and Redox Reactivity in Cr- and Fe-MOF-5. *J. Am. Chem. Soc.* **2013**, *135*, 12886−12891.

(40) Enemark, J. H.; Feltham, R. D. Principles of structure, bonding, and reactivity for metal nitrosyl complexes. *Coord. Chem. Rev.* **1974**, *13*, 339−406.

(41) Wright, A. M.; Hayton, T. W. Understanding the Role of Hyponitrite in Nitric Oxide Reduction. *Inorg. Chem.* **2015**, *54*, 9330−9341.

(42) Brozek, C. K.; Michaelis, V. K.; Ong, T.-C.; Bellarosa, L.; López, N.; Griffin, R. G.; Dincǎ, M. Dynamic DMF Binding in MOF-5 Enables the Formation of Metastable Cobalt-Substituted MOF-5 Analogues. *ACS Cent. Sci.* **2015**, *1*, 252−260.

(43) Osadchii, D. Y.; Olivos-Suarez, A. I.; Szécsényi, Á.; Li, G.; Nasalevich, M. A.; Dugulan, I. A.; Crespo, P. S.; Hensen, E. J. M.; Veber, S. L.; Fedin, M. V.; Sankar, G.; Pidko, E. A.; Gascon, J. Isolated Fe Sites in Metal Organic Frameworks Catalyze the Direct Conversion of Methane to Methanol. *ACS Catal.* **2018**, *8*, 5542−5548.

(44) Szécsényi, Á.; Li, G.; Gascon, J.; Pidko, E. A. Unraveling reaction networks behind the catalytic oxidation of methane with H_2O_2 over a mixed-metal MIL-53(Al,Fe) MOF catalyst. *Chem. Sci.* **2018**, *9*, 6765−6773.

(45) Stubbs, A. W.; Braglia, L.; Borfecchia, E.; Meyer, R. J.; Román-Leshkov, Y.; Lamberti, C.; Dincǎ, M. Selective Catalytic Olefin Epoxidation with MnII-Exchanged MOF-5. *ACS Catal.* **2018**, *8*, 596−601.

(46) Kresse, G.; Hafner, J. ABINITIO MOLECULAR-DYNAMICS FOR LIQUID-METALS. *Phys. Rev. B: Condens. Matter Mater. Phys.* **1993**, *47*, 558−561.

(47) Kresse, G.; Furthmuller, J. Efficient iterative schemes for ab initio total-energy calculations using a plane-wave basis set. *Phys. Rev. B: Condens. Matter Mater. Phys.* **1996**, *54*, 11169−11186.

(48) Perdew, J. P.; Burke, K.; Ernzerhof, M. Generalized gradient approximation made simple. *Phys. Rev. Lett.* **1996**, *77*, 3865−3868.

(49) Dudarev, S. L.; Botton, G. A.; Savrasov, S. Y.; Humphreys, C. J.; Sutton, A. P. Electron-energy-loss spectra and the structural stability of nickel oxide: An LSDA+U study. *Phys. Rev. B: Condens. Matter Mater. Phys.* **1998**, *57*, 1505−1509.

(50) Patton, D. C.; Pederson, M. R. Application of the generalized-gradient approximation to rare-gas dimers. *Phys. Rev. A: At., Mol., Opt. Phys.* **1997**, *56*, R2495−R2498.

(51) Zhang, Y.; Pan, W.; Yang, W. Describing van der Waals Interaction in diatomic molecules with generalized gradient approximations: The role of the exchange functional. *J. Chem. Phys.* **1997**, *107*, 7921−7925.

(52) Capdevila-Cortada, M.; Łodziana, Z.; López, N. Performance of DFT+U Approaches in the Study of Catalytic Materials. *ACS Catal.* **2016**, *6*, 8370−8379.

(53) Blöchl, P. E. Projector augmented-wave method. *Phys. Rev. B: Condens. Matter Mater. Phys.* **1994**, *50*, 17953−17979.

(54) Kresse, G.; Joubert, D. From ultrasoft pseudopotentials to the projector augmented-wave method. *Phys. Rev. B: Condens. Matter Mater. Phys.* **1999**, *59*, 1758−1775.

(55) Grimme, S. Semiempirical GGA-type density functional constructed with a long-range dispersion correction. *J. Comput. Chem.* **2006**, *27*, 1787−1799.

(56) Henkelman, G.; Uberuaga, B. P.; Jónsson, H. A climbing image nudged elastic band method for finding saddle points and minimum energy paths. *J. Chem. Phys.* **2000**, *113*, 9901−9904.

(57) Mori-Sánchez, P.; Cohen, A. J.; Yang, W. Many-electron self-interaction error in approximate density functionals. *J. Chem. Phys.* **2006**, *125*, 201102.

(58) Ruzsinszky, A.; Perdew, J. P.; Csonka, G. I.; Vydrov, O. A.; Scuseria, G. E. Density functionals that are one- and two- are not always many-electron self-interaction-free, as shown for H_2^+, He^{2+}, LiH^+, and Ne^{2+}. *J. Chem. Phys.* **2007**, *126*, 104102.

(59) Cohen, A. J.; Mori-Sánchez, P.; Yang, W. Insights into Current Limitations of Density Functional Theory. *Science* **2008**, *321*, 792.

(60) Haunschild, R.; Henderson, T. M.; Jiménez-Hoyos, C. A.; Scuseria, G. E. Many-electron self-interaction and spin polarization errors in local hybrid density functionals. *J. Chem. Phys.* **2010**, *133*, 134116.

(61) Zheng, X.; Liu, M.; Johnson, E. R.; Contreras-García, J.; Yang, W. Delocalization error of density-functional approximations: A distinct manifestation in hydrogen molecular chains. *J. Chem. Phys.* **2012**, *137*, 214106.

(62) Kim, M.-C.; Sim, E.; Burke, K. Understanding and Reducing Errors in Density Functional Calculations. *Phys. Rev. Lett.* **2013**, *111*, No. 073003.

(63) Schmidt, T.; Kümmel, S. One- and many-electron self-interaction error in local and global hybrid functionals. *Phys. Rev. B: Condens. Matter Mater. Phys.* **2016**, *93*, 165120.

(64) Gani, T. Z. H.; Kulik, H. J. Where Does the Density Localize? Convergent Behavior for Global Hybrids, Range Separation, and DFT+U. *J. Chem. Theory Comput.* **2016**, *12*, 5931−5945.

(65) Verma, P.; Truhlar, D. G. Does DFT+U mimic hybrid density functionals? *Theor. Chem. Acc.* **2016**, *135*, 182.

(66) Gani, T. Z. H.; Kulik, H. J. Unifying Exchange Sensitivity in Transition-Metal Spin-State Ordering and Catalysis through Bond Valence Metrics. *J. Chem. Theory Comput.* **2017**, *13*, 5443−5457.

(67) Janet, J. P.; Zhao, Q.; Ioannidis, E. I.; Kulik, H. J. Density functional theory for modelling large molecular adsorbate−surface interactions: a mini-review and worked example. *Mol. Simul.* **2017**, *43*, 327−345.

(68) Zhao, Q.; Kulik, H. J. Where Does the Density Localize in the Solid State? Divergent Behavior for Hybrids and DFT+U. *J. Chem. Theory Comput.* **2018**, *14*, 670−683.

(69) Gaggioli, C. A.; Stoneburner, S. J.; Cramer, C. J.; Gagliardi, L. Beyond Density Functional Theory: The Multiconfigurational Approach To Model Heterogeneous Catalysis. *ACS Catal.* **2019**, *9*, 8481−8502 and references therein. .

(70) He, Y.; Gräfenstein, J.; Kraka, E.; Cremer, D. What correlation effects are covered by density functional theory? *Mol. Phys.* **2000**, *98*, 1639−1658.

(71) Bochevarov, A. D.; Friesner, R. A. The densities produced by the density functional theory: Comparison to full configuration interaction. *J. Chem. Phys.* **2008**, *128*, No. 034102.

(72) Medvedev, M. G.; Bushmarinov, I. S.; Sun, J.; Perdew, J. P.; Lyssenko, K. A. Density functional theory is straying from the path toward the exact functional. *Science* **2017**, *355*, 49.

(73) Neese, F. The ORCA program system. *WIREs Comput. Mol. Sci.* **2012**, *2*, 73−78.

(74) Frisch, M. J.; Trucks, G. W.; Schlegel, H. B.; Scuseria, G. E.; Robb, M. A.; Cheeseman, J. R.; Scalmani, G.; Barone, V.; Mennucci, B.; Petersson, G. A.; Nakatsuji, H.; Caricato, M.; Li, X.; Hratchian, H. P.; Izmaylov, A. F.; Bloino, J.; Zheng, G.; Sonnenberg, J. L.; Hada, M.; Ehara, M.; Toyota, K.; Fukuda, R.; Hasegawa, J.; Ishida, M.; Nakajima, T.; Honda, Y.; Kitao, O.; Nakai, H.; Vreven, T.; Montgomery, J. A., Jr.; Peralta, J. E.; Ogliaro, F.; Bearpark, M.; Heyd, J. J.; Brothers, E.; Kudin, K. N.; Staroverov, V. N.; Kobayashi, R.; Normand, J.; Raghavachari, K.; Rendell, A.; Burant, J. C.; Iyengar, S. S.; Tomasi, J.; Cossi, M.; Rega, N.; Millam, N. J.; Klene, M.; Knox, J. E.; Cross, J. B.; Bakken, V.; Adamo, C.; Jaramillo, J.; Gomperts, R.; Stratmann, R. E.; Yazyev, O.; Austin, A. J.; Cammi, R.; Pomelli, C.; Ochterski, J. W.; Martin, R. L.; Morokuma, K.; Zakrzewski, V. G.; Voth, G. A.; Salvador, P.; Dannenberg, J. J.; Dapprich, S.; Daniels, A. D.; Farkas, Ö.; Foresman, J. B.; Ortiz, J. V.; Cioslowski, J.; Fox, D. J. *Gaussian09*, Revision D.01; Gaussian, Inc.: Wallingford CT, 2009.

(75) Weigend, F.; Ahlrichs, R. Balanced basis sets of split valence, triple zeta valence and quadruple zeta valence quality for H to Rn: Design an assessment of accuracy. *Phys. Chem. Chem. Phys.* **2005**, *7*, 3297−3305.

(76) Perdew, J. P.; Burke, K.; Ernzerhof, M. Errata: Generalized gradient approximation made simple. *Phys. Rev. Lett.* **1997**, *78*, 1396.

(77) Adamo, C.; Barone, V. Toward reliable density functional methods without adjustable parameters: The PBE0 model. *J. Chem. Phys.* **1999**, *110*, 6158−6169.

(78) Lee, C.; Yang, W.; Parr, R. G. Development of the Colle-Salvetti correlation-energy formula into a functional of the electron density. *Phys. Rev. B: Condens. Matter Mater. Phys.* **1988**, *37*, 785−789.

(79) Miehlich, B.; Savin, A.; Stoll, H.; Preuss, H. Results obtained with the correlation-energy density functionals of Becke and Lee, Yang and Parr. *Chem. Phys. Lett.* **1989**, *157*, 200−206.

(80) Becke, A. D. Density-functional thermochemistry. III. The role of exact exchange. *J. Chem. Phys.* **1993**, *98*, 5648−5652.

(81) Turner, S.; Lebedev, O. I.; Schroeder, F.; Esken, D.; Fischer, R. A.; Van Tendeloo, G. Direct imaging of loaded metal-organic

framework materials (metal@MOF-5). *Chem. Mater.* **2008**, *20*, 5622−5627.

(82) Ditchfield, R.; Hehre, W. J.; Pople, J. A. Self-Consistent Molecular-Orbital Methods. IX. An Extended Gaussian-Type Basis for Molecular-Orbital Studies of Organic Molecules. *J. Chem. Phys.* **1971**, *54*, 724−728.

(83) Hehre, W. J.; Ditchfield, R.; Pople, J. A. Self—Consistent Molecular Orbital Methods. XII. Further Extensions of Gaussian—Type Basis Sets for Use in Molecular Orbital Studies of Organic Molecules. *J. Chem. Phys.* **1972**, *56*, 2257−2261.

(84) Hariharan, P. C.; Pople, J. A. The influence of polarization functions on molecular orbital hydrogenation energies. *Theor. Chem. Acc.* **1973**, *28*, 213−222.

(85) Page, M. I.; Jencks, W. P. Entropic Contributions to Rate Accelerations in Enzymic and Intramolecular Reactions and the Chelate Effect. *Proc. Natl. Acad. Sci. U. S. A.* **1971**, *68*, 1678.

(86) Walsh, A.; Sokol, A. A.; Buckeridge, J.; Scanlon, D. O.; Catlow, C. R. A. Oxidation states and ionicity. *Nat. Mater.* **2018**, *17*, 958−964.